GPS Solutions (2024) 28:128
https://doi.org/10.1007/s10291-024-01669-9

ORIGINAL ARTICLE

Risk overbounding for ionospheric gradient monitor using geometry-free double differenced carrier phase measurements

Wang Li[1] · Yiping Jiang[1]

Received: 13 April 2023 / Accepted: 3 May 2024
© The Author(s) 2024

Abstract
Ionosphere anomaly can cause large spatial gradients in the double-differenced carrier phase (DDCP) measurements. Taking advantage of this characteristic, the ionospheric gradient monitor (IGM) is designed with multiple ground reference stations to detect threatening ionospheric gradients for safety of life applications. An optimal IGM should be most sensitive to ionospheric gradients and least sensitive to other errors. However, current IGM suffers from the influence of tropospheric error, which can degrade monitor performance under extreme weather conditions by causing risks of false alarms and missed detections. To address this issue, an alternative IGM is proposed using the geometry-free combination of DDCP as the test statistic. Ambiguity resolution procedure is designed for estimating the ambiguity term in the test statistic. The risk induced by the wrong ambiguity fix and tropospheric error are analyzed and bounded with required averaging period and minimum baseline length. The results show that the proposed theoretical IGM is capable of achieving probability of false alarm of 10^{-8} and probability of missed detection of 10^{-6} with a filtering period of 612 s and baseline length of 371.7 m or a filtering period of 544 s and baseline length of 384.4 m. The experimental results using data collected from Hong Kong Satellite Positioning Reference Station Network demonstrate that the performance of the proposed theoretical IGM is comparable to that of the existing detection algorithm.

Keywords GNSS · Ionospheric gradient monitor · Tropospheric anomaly · Risk overbounding

Introduction

An ionospheric anomaly can result in large spatial and temporal decorrelations between the ground subsystem and the airborne receiver. This makes it unpredictable and challenging for integrity monitoring, especially at low latitudes with more active ionosphere behavior. The spatial gradient is modeled as a linear front with a unit of millimeters per kilometer (Lee et al. 2017; Luo et al. 2004). The magnitude of spatial gradient varies greatly between nominal and abnormal conditions. Under nominal conditions, the spatial gradient is on the order of several millimeters per kilometer of separation between receivers. However, under ionospheric anomaly, it can reach hundreds of millimeters per kilometer (Pullen 2000; Pullen et al. 2009). For example, in the Conterminous United States (CONUS), the nominal value of ionospheric spatial gradients is approximately 4 mm/km (Lee et al. 2017), while during anomalous conditions, an ionospheric spatial gradient larger than 400 mm/km has been observed in the CONUS (Pullen et al. 2009). Such a large gradient can result in significant positioning error at user's position. To exclude the faulty satellite before being used for relative positioning, ionosphere monitors that are sensitive to the ionospheric gradient are designed.

Like the payload code-carrier divergence (CCD) fault, ionosphere anomaly also results in a divergence between code and carrier. The CCD monitor implemented both in ground and airborne subsystems can also be used to detect an ionosphere gradient with a certain velocity (Brenner and Liu 2010; Jiang et al. 2017). Furthermore, a relative ionospheric gradient monitor (IGM) that is not dependent on the history of measurements was designed using double differenced carrier phase (DDCP) measurements as the test statistics (Jing et al. 2012; Khanafseh et al. 2012; Belabbas and Meurer 2012; Reuter et al. 2012). For simplicity, the relative IGM is referred to as IGM in the following text. The

✉ Yiping Jiang
yiping.jiang@polyu.edu.hk

[1] Department of Aeronautical and Aviation Engineering, The Hong Kong Polytechnic University, Hung Hom, Hong Kong, SAR, China

Published online: 21 May 2024

DDCP is formed by two reference stations observing two satellites (one reference satellite and one non-reference satellite). A fault-free satellite is chosen as the reference satellite by another "executive" monitor based on the assumption that the ionospheric gradient does not impact all satellites. This assumption is considered as reasonable for a few reasons: 1, typically worst case ionospheric gradient for GBAS are gradients that my happened between the user and the reference stations, and thus unlikely to impact all satellites at the same time geometrically; 2, even if the ionospheric gradient impacts all satellites equally, then it will be common and similar to a receiver clock bias (therefore, either estimated as such, or eliminated in the differential process); 3, since the IGM is applied utilizing snapshot estimation process, there is no memory or filter of previous faults, and therefore, the previous point stands; 4, if it is impacting all satellites but in different magnitudes, then as long as the difference is smaller than the threshold, the effect on position domain is smaller than the alert limit. Based on the assumption that the reference satellite is not affected by the ionospheric gradient or ionospheric fault, the IGM determines whether the non-reference satellite is affected by the ionospheric gradient by comparing the DDCP test statistics with its threshold. The IGM issues an alert for the non-reference satellite when its test statistics exceed the threshold. All non-reference satellites are monitored by the same process one by one independently. In other words, the IGM is able to detect the satellites affected by the ionospheric gradients even when most satellites are affected by the gradients.

The IGM plays an important role in limiting the magnitude of differential range error when other monitors fail to detect the ionospheric anomaly that is almost stationary relative to the reference station (Harris et al. 2011). However, the DDCP formed by a reference satellite and a non-reference satellite (NRS) in IGM assumes that the reference satellite (RS) is fault-free. In other words, the IGM cannot distinguish whether the detected fault is on the RS or on the NRS. To address this issue, Jiang et al. (2023) proposed a method that uses multiple hypotheses to detect the fault on both the RS and NRS simultaneously.

Currently, only GPS L1 measurements are used in civil aviation, and L2 frequency is not employed by civil aviation because it is not in an aeronautical radionavigation service band (Marini-Pereira et al. 2021). The GPS L5 and Galileo E5 signals have been approved for use in civil aviation and will be applied to civil aviation in the future (Circiu et al. 2017). With dual-frequency measurements, smoothing techniques including the ionosphere-free (IFree) and divergence-free are considered to remove the first-order ionospheric effect (Hwang et al. 1999). The cost with dual-frequency techniques is the inflated position error (Felux et al. 2015). To address this issue, a feasible solution is to continue using single frequency for positioning in the nominal case and the dual-frequency solution is only adopted when ionosphere monitors trigger any alarm (Felux et al. 2017). For integrity monitoring, dual-frequency signals can be used to enhance the monitor performance by exploring frequency diversity. For example, a wide-lane (WL) combination of DDCP measurements was proposed as the test statistic of IGM (Patel et al. 2020). The WL ambiguity is easier to be resolved than the L1 ambiguity for newly acquired and re-acquired satellites. However, the standard deviation of test statistics is also inflated, making it more difficult to meet the integrity requirement.

After compensating the residual range by the surveyed position of reference stations, the DDCP measurements still contain residual ionospheric error, tropospheric error, ephemeris error, multipath and noise. If a satellite is impacted by an ionosphere anomaly, troposphere anomaly, or ephemeris fault, a spatial gradient is generated in the DDCP measurements. With the single fault assumption, the probability that an ionospheric fault and an ephemeris fault occur at the same time in one satellite is considered negligible. Hence, the residual ephemeris error is assumed as nominal and on the order of a few centimeters.

Under dry weather conditions, the residual tropospheric error is small and can be well modeled, while the behavior of tropospheric anomaly cannot be accurately described by a Gaussian distribution. Troposphere anomaly happens under extreme weather conditions such as thunderstorms, and their prior probability varies with weather, location, and season. Since the troposphere is located in the lower atmosphere, it can impact multiple satellites at the same time. Therefore, the probability that an ionosphere anomaly and a troposphere anomaly exist at the same time in one satellite cannot be neglected. Based on previous observations, the troposphere anomaly is not hazardous enough to be characterized as a threat to users (Alexander et al. 2014; van Graas and Zhu 2011; Guilbert et al. 2017). However, the spatial gradient in DDCP measurement caused by the tropospheric anomaly can induce extra risk which is not considered in the design of current IGM.

When reference stations have similar heights, there is no need to consider the vertical variation of water vapor under extreme weather conditions. The distance between reference stations is typically shorter than the airport runway length, e.g., less than 5 km. However, based on the current measurement of the horizontal variation of water vapor under extreme weather conditions, the possibility of a large troposphere anomaly within this distance cannot be ignored. For example, International Civil Aviation Organization (ICAO) reported an unexpected atmospheric behavior pointing to the non-modeled tropospheric error with a magnitude of around 115 mm/km in the DDCP measurements (Alexander et al. 2014). Also, a tropospheric spatial decorrelation error of 41 cm caused by tropospheric anomaly was observed over

a 5 km baseline near Athens, OH (van Graas and Zhu 2011; Huang and van Graas 2006; Huang et al. 2008). In addition to the extra risk of false alarms (FA), the tropospheric anomaly occurring at the same time as the ionospheric anomaly with gradients of opposite signs can also result in the risk of missed detections (MD).

Various methods have been proposed to bound the risk induced by troposphere anomaly in IGM. One intuitive way is to increase the standard deviation of the test statistics. However, this can degrade the monitor performance by increasing the probability of FA (P_{FA}) and probability of MD (P_{MD}) (Khanafseh et al. 2012). Another method is to use the 'time-interval' monitor, which distinguishes between the tropospheric and the ionospheric gradients by observing the characteristics of the accumulated carrier phase errors when a gradient is detected by the IGM (Jing et al. 2014). However, the 'time-interval' is not a real-time monitor as it involves a detection delay after the fault occurs. A different method involves using two parallel baselines that are 1 km apart, considering that tropospheric anomaly is more often perceived as a local phenomenon than ionospheric error (Patel et al. 2020; Jiang 2020). However, with the tradeoff relationship between continuity and integrity, this method improves service continuity by scarifying service integrity.

To overcome the limitations of previous methods, a geometry-free (GF) combination of DDCP measurements is proposed in this paper as the test statistic with tropospheric error removed from the test statistic. Although the risk of tropospheric error in the test statistics is eliminated, the ambiguity in the test statistics is not separable from the tropospheric gradient under troposphere anomaly. Therefore, this paper designs the methodology of bounding the risk of wrong ambiguity fix in order to meet the required P_{FA} and P_{MD}.

First, the GF test statistic of IGM is described. Then, to resolve the ambiguity in the test statistic, an integer ambiguity method is examined with derived performance minimum to meet the CAT III requirements. The residual tropospheric error induced by the maximum observed tropospheric gradient and the extra risk caused by wrong ambiguity resolution are constrained in the integer ambiguity method. Finally, we present the final remarks and conclusions.

Geometry-free test statistic

Figure 1 depicts an aircraft during its landing approach towards a runway, following a glide path angle and reaching a glide path intercept point (GPIP). The aircraft requires fault-free measurements for positioning at the decision height (H) which is typically 5 km from GPIP. Two antennas

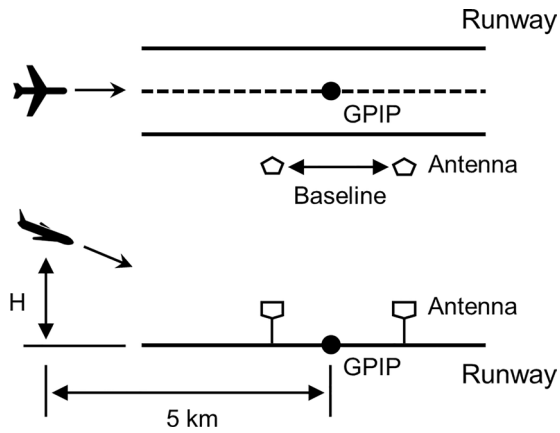

Fig. 1 Illustration of landing approach and antenna baseline configuration

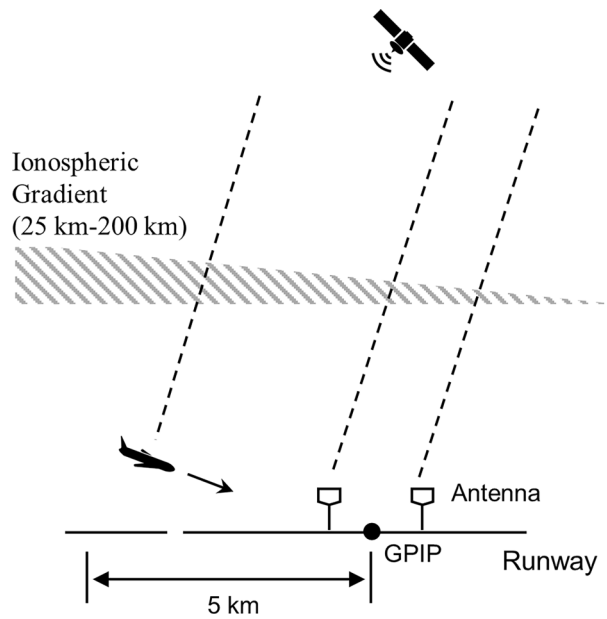

Fig. 2 Side-view of an aircraft and an ionospheric spatial gradient

forming a baseline of hundreds of meters parallel to the runway are used to detect the threatening ionospheric gradient along the direction of runway.

The ionospheric spatial gradient, i.e., spatial decorrelation, is modelled as a linear change in vertical ionospheric delay as shown in Fig. 2. The typical range of the gradient width is from 25 to 200 km, and the magnitude of a threatening gradient is larger than 200 mm/km (Luo et al. 2004). Since the distance among the aircraft and ground antennas is much smaller compared with the distance to satellites, the satellite signals of aircraft and ground antennas are approximately parallel. Considering the direction of anomalous ionosphere gradient is along the runway and

ground antennas are installed at the end of the runway, if the anomalous ionosphere gradient impacts the ground antennas, the aircraft is very likely to be impacted by the same anomalous ionosphere gradient. In other words, the ionospheric gradient measured by the antennas can reflect the gradient that affects the aircraft.

After double-differencing between two satellites and two reference receivers with baseline around several hundred meters, the common errors such as satellite and antenna phase center variation and phase wind-up correction are canceled in the DDCP measurements. Using precisely surveyed coordinates of the ground receivers, the geometric range is compensated beforehand. The residual errors in the DDCP measurement are expressed as,

$$\phi_1 = \lambda_1 N_1 - I_1 + Tr + E + \varepsilon_{\phi_1} \tag{1}$$

where ϕ_1 is the DDCP measurement of L1 frequency with the subscript used to note the frequency; λ_1 is the wavelength of L1 signal; N_1 is the integer ambiguity of L1 DDCP; I_1 is the residual ionospheric error; Tr is the residual tropospheric error; E is the residual ephemeris error; ε_{ϕ_1} is the residual multipath and noise with a standard deviation (sigma) of σ_p. Since the baseline between two ground reference receivers is parallel to the runway, the residual ionospheric error can be approximated by the product of the ground baseline length x_{ab} and magnitude of ionospheric gradient g_{iono} (Luo et al. 2004). Although the true ionospheric gradient cannot be obtained due to the existence of multipath and noise, the DDCP can reflect the ionospheric gradient condition. In particular, the DDCP is larger when the ionospheric delays between the antenna are less correlated (a larger g_{iono}), which also indicates a larger g_{iono} between the aircraft and the ground facility. Therefore, based on DDCP as the test statistic, the relative IGM is able to issue alerts for threatening gradients when DDCP exceeds the pre-defined threshold. The errors of multipath and noise are considered into the pre-defined threshold by meeting required P_{FA}.

In order to mitigate the impact of residual tropospheric error, the GF combination of DDCP measurements is proposed as the test (ts) statistic of the IGM,

$$ts = \phi_5 - \phi_1 - \left(\lambda_5 N_5 - \lambda_1 N_1\right) = \left(\frac{\lambda_1^2 - \lambda_5^2}{\lambda_1^2}\right) I_1 + \varepsilon_{\phi_5} - \varepsilon_{\phi_1} \tag{2}$$

where both T and E are eliminated by the difference.

Considering the correlation between L1 and L5 signals, the sigma of $\varepsilon_{\phi_5} - \varepsilon_{\phi_1}$ can be bounded by $\sigma_{ts} \le \sqrt{2}\sigma_p$, assuming the sigma of ε_{ϕ_1} and ε_{ϕ_5} are the same. With the antenna phase variation calibrated, σ_p is overbounded as 0.6 cm (Khanafseh et al. 2012), and σ_{ts} is bounded by 0.85 cm. With the tropospheric error and ephemeris error eliminated in the GF combination, the residual ionospheric error results in a spatial gradient that can be used to detect the ionospheric anomaly on the condition that the ambiguity term $\lambda_5 N_5 - \lambda_1 N_1$ can be estimated with sufficiently high precision.

Integer ambiguity method

The integer ambiguity method addresses the issue of fixing the ambiguities by recovering the integer nature of N_1 and N_5. This method has the advantage that no extra noise is introduced from ambiguity estimation process to the test statistic. A cascaded integer ambiguity method is proposed for ephemeris monitor with L1 DDCP as the test statistics (Jiang 2020). The WL ambiguity N_w ($N_w = N_1 - N_5$) is estimated first, followed by the estimation of N_1 (Jiang 2020). With its performance demonstrated to be better than other methods, this method is adopted herein. First, N_w is estimated by the Hatch-Melbourne-Wübbena (HMW) combination (Patel et al. 2020; Jiang 2020),

$$v_w = \frac{\phi_w - R_n}{\lambda_w} = N_w + \frac{f_1\varepsilon_{\phi_1} - f_5\varepsilon_{\phi_5}}{(f_1 - f_5)\lambda_w} - \frac{f_1\varepsilon_{R_1} + f_5\varepsilon_{R_5}}{(f_1 + f_5)\lambda_w} \tag{3}$$

where v_w is the HMW combination; $\phi_w = \frac{f_1\phi_1 - f_5\phi_5}{f_1 - f_5}$ is the WL phase combination of DDCP measurements with f_1 and f_5 as the frequencies of L1 and L5 signals, respectively; $R_n = \frac{f_1 R_1 + f_5 R_5}{f_1 + f_5}$ is the narrow-lane combination of double-differenced code measurements of L1 and L5 frequencies (R_1 and R_5); ε_{R_1} and ε_{R_5} are the residual multipath and noise in R_1 and R_5, respectively; The sigma of ε_{R_1} and ε_{R_5} denoted as σ_c is assumed to be the same and bounded by 84 cm (Khanafseh et al. 2017). $\lambda_w = \frac{c}{f_1 - f_5}$ is the WL wavelength with c as the speed of light; v_w is free of ionospheric, tropospheric, and ephemeris errors, and the residual multipath and noise in v_w can be effectively reduced by averaging among multiple epochs. The sigma of the dominating code error in (3) is bounded by $\sigma_{cn} \le \frac{\sqrt{f_1^2 + f_5^2}}{(f_1 + f_5)\lambda_w}\sigma_c$ assuming independency between L1 and L5 code measurements. With σ_c bounded by 84 cm, σ_{cn} can then be bounded by 60 cm.

The probability of correctly fixing N_w indicated by $P(CF_w)$ is expressed as,

$$P(CF_w) = P\left(\left|v_w - N_w\right| < \frac{1}{2}\right) \tag{4}$$

where $v_w - N_w$ follows a zero mean Gaussian distribution with sigma of σ_{cn}.

After the WL integer ambiguity is estimated as $\hat{N}_w$, N_1 is then estimated by an IFree statistic,

$$v_1 = \frac{f_1^2\phi_1 - f_5^2\phi_5 - f_5^2\lambda_5\hat{N}_w}{f_1^2\lambda_1 - f_5^2\lambda_5} = N_1 + \frac{f_1^2 - f_5^2}{f_1^2\lambda_1 - f_5^2\lambda_5}(Tr + E) + \frac{f_1^2\varepsilon_{\phi_1} - f_5^2\varepsilon_{\phi_5}}{f_1^2\lambda_1 - f_5^2\lambda_5} \tag{5}$$

where v_1 is formed to eliminate the ionospheric component; the sigma of the residual multipath and error in (5) is bounded by $\sigma_{pg} \le \frac{\sqrt{f_1^4+f_5^4}}{f_1^2\lambda_1 - f_5^2\lambda_5}\sigma_p$. With σ_p bounded by 0.6 cm, σ_{pg} is then bounded by 14.3 cm. The probability of correctly fixing N_1 based on a correctly fixed N_w indicated by $P(CF_1|CF_w)$ is,

$$P(CF_1|CF_w) = P\left(\left|v_1 - N_1\right| < \frac{1}{2}\right) \tag{6}$$

where $v_1 - N_1$ follows a zero mean Gaussian distribution with sigma of σ_{pg}.

The dominating error in (3) is code multipath and noise, which is independent of the residual errors in (5). Assuming the independence between (3) and (5), the probability of correctly fixing N_1 denoted as $P(CF_1)$ is expressed as,

$$P(CF_1) = P(CF_1|CF_w)P(CF_w) \tag{7}$$

As N_5 is determined by $N_5 = N_1 - N_w$, the probability of correctly fixing N_5 is equal to $P(CF_1)$.

During the ambiguity resolution process, the wrong ambiguity fixes of N_w and N_1, i.e., IF_w and IF_1 can cause risks of false alarm and missed detection by deviating the distribution of the test statistics from zero. These risks should be considered and bounded by selecting appropriate averaging time. It should be noted that although the tropospheric effect is eliminated in the test statistics, it persists in N_1 estimation. To constrain the troposphere-induced risk under extreme weather conditions on v_1, the worst-case tropospheric anomaly is accounted for as a bias. The troposphere gradient of 115 mm/km is adopted in this study (Alexander et al. 2014). Considering the ephemeris error and troposphere error are not separable within the DDCP measurement, the residual nominal ephemeris error is assumed to be already included in the troposphere gradients. The magnitude of the tropospheric gradient is denoted as g_{trop}. Both the tropospheric and ionospheric errors increase with the increase of baseline length. Larger ionospheric errors can be more easily detected, whereas larger tropospheric errors are not desirable for ambiguity resolution.

In order to bound the risk of wrong ambiguity fix, a single threshold and a multiple threshold method are proposed. The former uses a single threshold region, while the latter contains multiple threshold regions to allow several incorrect fix (IF) events to be distinguished from the FA. Both methods are described below in two aspects: (1) risk allocation for allocating the total required P_{FA} and P_{MD} onto each individual risk; (2) risk overbounding for deriving the required averaging time and ground baseline length to meet these required risks.

Risk overbounding using single threshold method

Bounding risk of false alarm

Under the fault-free hypothesis, the probability of FA (P_{FA}) is defined by the probabilities under both correct fix (CF) and IF of N_1,

$$P_{FA} = P\{|t| > T|H_0\} = P(FA|CF)P_{CF} + P(FA|IF)P_{IF} \tag{8}$$

where $P_{CF} = P(CF_1)$ and P_{IF} is the probability of any IF event, either N_w or N_1, with $P_{CF} + P_{IF} = 1$; T is single threshold. To save the complexity of computing $P(FA|IF)$, P_{FA} can be conservatively bounded by,

$$P_{FA} \le P(FA|CF)\left(1 - P_{IF}\right) + P_{IF} \tag{9}$$

where ts under CF follows a zero mean Gaussian distribution with sigma of σ_{ts}, and $P(FA|CF)$ can be computed from the Gaussian cumulative distribution function given T.

To meet the P_{FA} requirement, an optimal risk allocation between $P(FA|CF)$ and P_{IF} is attempted by defining a varying k_1 factor with $0 \le k_1 \le 1$,

$$P_{IF} = k_1 P_{FA} \tag{10}$$

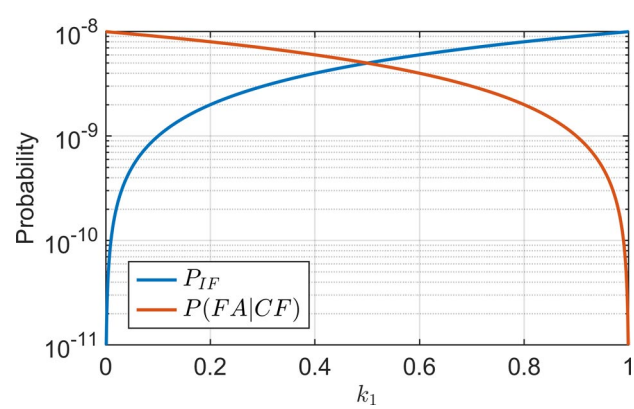

Fig. 3 P_{IF} and $P(FA|CF)$ versus k_1 with the single threshold method

The probability allocated to $P(FA|CF)$ and P_{IF} as a function of k_1 is illustrated in Fig. 2 given of P_{FA} of 10^{-8}.

As validated by Fig. 3, although the risk distribution between P_{IF} and $P(FA|CF)$ is different from the simple linear allocation of the sum of P_{IF} and $P(FA|CF)$ onto these two risks, the interception point of equal allocation is the same when $1 - P_{IF}$ is small enough to be negligible. P_{IF} is further allocated between two IF events of $P(IF_w) = 1 - P(CF_w)$ and $P(IF_1) = 1 - P(CF_1|CF_w)$,

$$\begin{aligned} P_{IF} &= 1 - P(CF_1|CF_w)P(CF_w) \\ &= P(IF_w) + P(IF_1) - P(IF_w)P(IF_1) \end{aligned} \tag{11}$$

Similarly, to obtain an optimal allocation, a k_2 factor is defined as,

$$P(IF_1) = k_2 P_{IF} \tag{12}$$

With $P(IF_w) - P(IF_w)P(IF_1) \geq 0$ in (11), the range of k_2 can also be limited by $0 \leq k_2 \leq 1$. The results of risk allocation with different k_1 given and $k_2 = 0.5$ are illustrated in Fig. 4.

After risk allocation, the P_{FA} bounding process is described as follows. First, the threshold is determined by $T = \Phi^{-1}\left(1 - \frac{P(FA|CF)}{2}\right)\sigma_{ts}$ to meet the allocated risk on $P(FA|CF)$. To bound P_{IF} with an allocated probability, v_1 and v_w are averaged among multiple epochs to suppress the residual multipath and noise. The resulted $P(CF_{N_w})$ and $P(CF_{N_1}|CF_{N_w})$ can be computed as follows,

$$P(CF_{N_w}) = \Phi\left(\frac{\frac{1}{2}}{\hat{\sigma}_{cn}}\right) - \Phi\left(\frac{-\frac{1}{2}}{\hat{\sigma}_{cn}}\right) \tag{13}$$

$$P(CF_{N_1}|CF_{N_w}) = \Phi\left(\frac{\frac{1}{2} - \delta_{trop}}{\hat{\sigma}_{pg}}\right) - \Phi\left(\frac{-\frac{1}{2} - \delta_{trop}}{\hat{\sigma}_{pg}}\right) \tag{14}$$

where $\hat{\sigma}_{cn} \leq \frac{\sigma_{cn}}{\sqrt{n_w}}$ and $\hat{\sigma}_{pg} \leq \frac{\sigma_{pg}}{\sqrt{n_1}}$ are the sigma of v_w and v_1 after averaging among multiple epochs, respectively. The number of required epochs denoted as n_w and n_1, can then be determined by the allocated risk. Under extreme weather conditions, the residual troposphere error in v_1 cannot be effectively reduced by averaging, which is accounted for as a bias and computed by $\delta_{trop} = \frac{f_1^2 - f_5^2}{f_1^2\lambda_1 - f_5^2\lambda_5} Tr$ derived from (5). Similar to the ionospheric error, the tropospheric error Tr is expressed by the product of the tropospheric gradient g_{trop} and the baseline length x_{ab}. Therefore, δ_{trop} is equal to $\frac{f_1^2 - f_5^2}{f_1^2\lambda_1 - f_5^2\lambda_5} g_{trop} x_{ab}$. Additionally, the tropospheric bias needs to be constrained by $\left|\delta_{trop}\right| < \frac{1}{2}$ such that a large enough $P(CF_{N_1}|CF_{N_w})$ can be obtained after averaging.

Assuming $k_1 = k_2 = 0.5$, n_w is derived as 91 by (13), and n_1 is searched in (14) with various g_{trop} and x_{ab} as shown in Fig. 5. As shown in Fig. 3, n_1 increases with the increase of both g_{trop} and x_{ab}. Therefore, the historically observed worst g_{trop} (115 mm/km) is used for bounding δ_{trop}, and a maximum x_{ab} is searched for constraining the $P(IF_1)$.

Bounding risk of missed detection

On the other hand, increasing x_{ab} enhances the monitor's sensitivity to ionospheric anomaly. The minimum x_{ab} is searched for meeting the requirement of the probability of MD (P_{MD}) under the faulty hypothesis,

$$\begin{aligned} P_{MD} &= P\{|ts| < T|H_a\} \\ &= P(MD|CF)P_{CF} + P(MD|IF)P_{IF} \end{aligned} \tag{15}$$

Considering P_{CF} is much larger than $P(MD|CF)$, P_{MD} can be bounded by,

$$P_{MD} \leq P(MD|CF) + P(MD|IF)P_{IF} \tag{16}$$

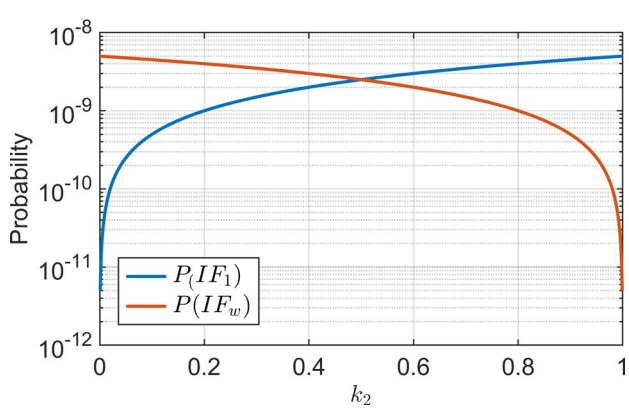

Fig. 4 $P(IF_1)$ and $P(IF_w)$ as functions of k_2 given $k_1 = 0.5$

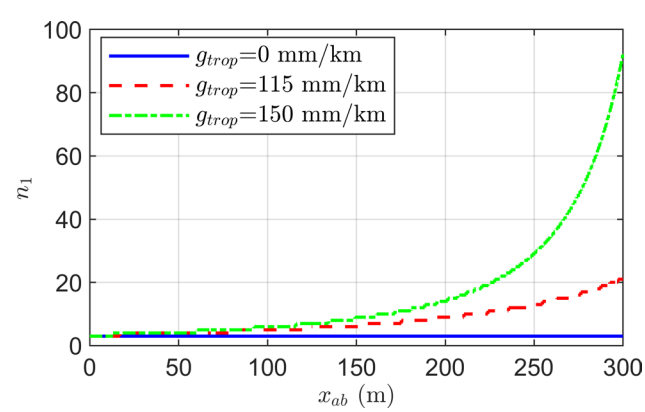

Fig. 5 n_1 with the single threshold method

Given that $P(MD|IF)P_{IF} \leq P_{IF}$ has already been bounded by averaging, only $P(MD|CF)$ needs to be bounded. $P(MD|CF)$ indicates P_{MD} under CF and is computed by the cumulative probability of the test statistic lies inside the threshold region. Under the faulty hypothesis, the distribution of the test statistic is biased by the ionospheric anomaly which is computed by the product of ionospheric gradient g_{iono} and the baseline length x_{ab}. In order to ensure the allocated $P(MD|CF)$ can be satisfied, the baseline length needs to long enough to meet the requirement. The minimum baseline length x_{ab} to bound $P(MD|CF)$ can be computed by,

$$x_{ab} \geq \frac{\lambda_1^2 D_{ga}}{(\lambda_5^2-\lambda_1^2)Er}\left[\Phi^{-1}\left(1-\frac{P(FA|CF)}{2}\right)+\Phi^{-1}(1-P(MD|CF))\right]\sigma_{ts} \tag{17}$$

where Φ^{-1} is the inverse of the standard normal cumulative distribution. D_{ga} is the distance between the reference station and the user. Taking the Ground Based Augmentation System (GBAS) as an example, D_{ga} varies when the aircraft is approaching to the ground station; (Pervan and Chan 2003). In CAT III GBAS, the probability that an undetected ionospheric front leading to Er greater than 2.75 m must not exceed 10^{-9}. With a presumed prior probability of a potentially hazardous ionospheric gradient as 10^{-3} (Yoon et al. 2020), IGM needs to meet a P_{MD} requirement at 10^{-6}.

The maximum D_{ga} is 9 km, which is a sum of the distance between the landing threshold point and the ground station plus the ionospheric travel distance (Patel et al. 2020). With the increase of D_{ga}, δ decreases and results in an increase of P_{MD}. Similarly, a smaller Er results in larger P_{MD}. Thereby, using the upper limit of D_{ga} (9 km) and lower limit of Er (2.75 m) are conservative for meeting the P_{MD} requirements.

With k_1 determined, the risk allocation on P_{IF} and $P(FA|CF)$ can be obtained with (9), and also the risk allocation on $P(MD|CF)$ with (16). Therefore, the minimum x_{ab} can be obtained as a function of k_1 with (17) as shown in Fig. 6,

As shown in Fig. 6, the required minimum x_{ab} increases from 368 to 405 m as k_1 increases from 0 to 1. In addition to the baseline length, the required number of epochs for averaging also needs to be considered. The determination of n_1 hinges on $P(IF_1)$, which is allocated by k_1 and k_2 for distributing P_{FA} to $P(IF_1)$, and x_{ab}, which needs to satisfy $P(MD|CF)$ and is determined by k_1 that allocates P_{MD} to $P(MD|CF)$). The relationship between the total epochs required for averaging, i.e., $n_w + n_1$, as a function of k_1 and k_2 is shown in Fig. 7.

The results of n_1 and n_w in Fig. 7 are obtained to bound the probability allocated to P_{IF} considering the maximum g_{trop} of 115 mm/km. The minimum total epochs required for averaging are found through Fig. 5 as 153 [the required averaging time t_a of 612 s assuming a time constant of 2 s (Jiang 2020)], and the corresponding required threshold and baseline length are 4.97 cm and 371.7 m, respectively. The minimum required baseline length of 371.7 m is determined by the allocated P_{MD} while the maximum baseline length of 473.6 m is determined by limiting $\left|\delta_{trop}\right| < \frac{1}{2}$. Note that the above conclusion is based on the maximum g_{trop} of 115 mm/km. Considering a potentially g_{trop} larger than 115 mm/km, the required averaging time will increase. In particular, when g_{trop} exceeds 147 mm/km, the required averaging time will be infinite. That is, cannot be correctly fixed since the troposphere-induced error in estimation is larger than 0.5, i.e.,.

The allocation of probability and determination of overbounging parameters are summarized in Fig. 8.

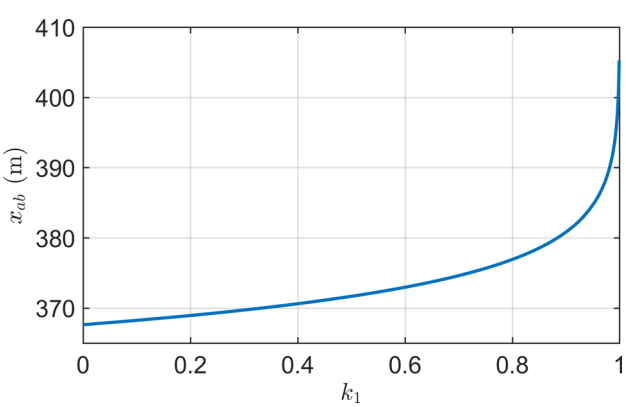

Fig. 6 x_{ab} versus k_1 with the single threshold method

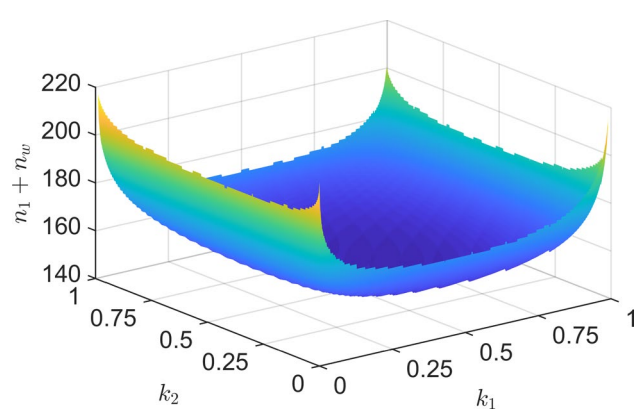

Fig. 7 Total epochs required for averaging with the single threshold method given g_{trop} of 115 mm/km

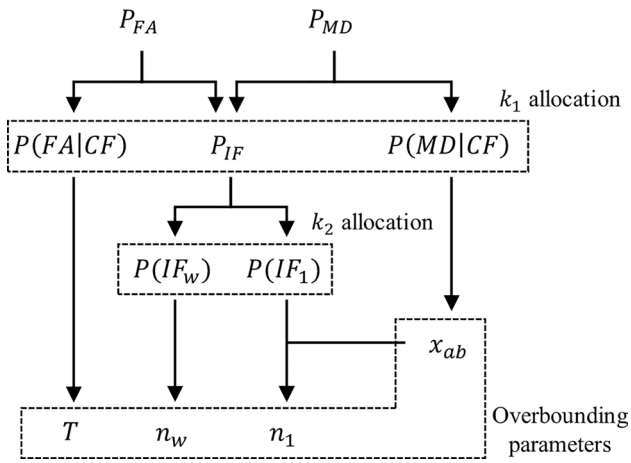

Fig. 8 Probability allocation and the bounding parameters with the single threshold method

Risk overbounding using multiple threshold method

Bounding risk of false alarm

The single threshold method utilizes the mutual exclusivity of P_{CF} and P_{IF} to simplify the overbounding without the necessity to consider specific IF events. In order to further relax the requirement on averaging time, a multiple threshold method is devised to limit false alarm conditions under a few IF events (Patel et al. 2020; Khanafseh and Langel 2011; Khanafseh and Pervan 2008). Considering two IF events, i.e., $N_w - \hat{N}_w = \pm 1$, the induced bias in N_1 estimation is $\pm\frac{f_5^2\lambda_5}{f_1^2\lambda_1 - f_5^2\lambda_5} = \pm 2.95$. After rounding to the nearest integer, the induced integer in N_1 and N_5 estimation and the induced bias in test statistics μ are illustrated in Table 1,

The P_{FA} with multiple threshold method under fault-free hypothesis is expressed as,

$$P_{FA} \le P(|ts| \succ T|CF)P_{CF} + P\left(|ts| \succ T|IF_w^1\right)P_{IF_w^1} + P\left(|ts| \succ T|IF_w^{-1}\right)P_{IF_w^{-1}} + \left(1 - P_{CF} - P_{IF_w^1} - P_{IF_w^{-1}}\right) \tag{18}$$

where $|ts| \succ T$ denotes the FA regions defined as,

Table 1 Induced integer and bias with a wrong N_w

Event	IF_w^1	CF	IF_w^{-1}
$\hat{N}_w$	$N_w + 1$	N_w	$N_w - 1$
$\hat{N}_1$	$N_1 - 3$	N_1	$N_1 + 3$
$\hat{N}_5$	$N_5 - 4$	N_5	$N_5 + 4$
μ	$4\lambda_5 - 3\lambda_1$ (44.84 cm)	0 cm	$3\lambda_1 - 4\lambda_5$ (– 44.84 cm)

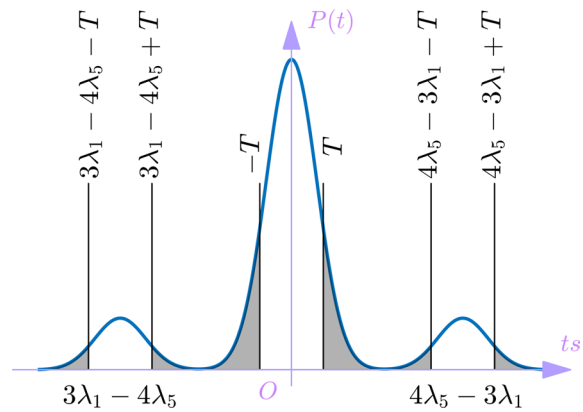

Fig. 9 False alarm regions with the multiple threshold method, the grey areas represent the FA regions

$$\{|ts| \succ T\} \triangleq \left\{T < |ts| < 4\lambda_5 - 3\lambda_1 - T\right\} \cup \left\{|ts| > 4\lambda_5 - 3\lambda_1 + T\right\} \tag{19}$$

The definition of the multiple threshold regions is based on the induced bias listed in Table 1.

In the single threshold method, any event with the test statistic exceeding the threshold is regarded as a FA. With the multiple threshold method, the FA region is narrowed down to allow two IF events, i.e., IF_w^1 and IF_w^{-1}, to be distinguished from the FA events. The mixed Gaussian distribution with the multiple threshold method is illustrated in Fig. 9, where the grey areas represent the FA regions.

The middle two terms of (18) can be bounded by $P\left(|ts| \succ T|IF_w^1\right)P_{IF_w^1} \le P_{IF_w^1}$, $P\left(|ts| \succ T|IF_w^{-1}\right)P_{IF_w^{-1}} \le P_{IF_w^{-1}}$. Furthermore, with P_{CF} much larger than $P(|ts| \succ T|CF)P_{CF}$, the first term is bounded as $P(|ts| \succ T|CF)P_{CF} \le P(|ts| \succ T|CF)$. To further simplify the allocation process from the total P_{FA} onto each item, it is assumed that the prior probabilities of the two IF events are the same, i.e., $P_{IF_w^1} = P_{IF_w^{-1}}$. Therefore, an optimal risk allocation can be attempted by defining two varying factors of j_1 and j_2,

$$P_{IF_w^1} = j_1 P_{FA} \tag{20}$$

$$P(|ts| \succ T|CF) = j_2 P_{FA} \tag{21}$$

where $0 \le j_1 \le 1$ and $0 \le j_2 \le 1$.

After risk allocation, the P_{FA} bounding process is described as follows. First, the $P(|ts| \succ T|CF)$ is similarly bounded by the threshold region using $\Phi^{-1}\left(1 - \frac{P(|ts| \succ T|CF)}{2}\right)\sigma_{ts}$. This threshold is also used to constrain the FA regions in both $P\left(|ts| \succ T|IF_w^1\right)$ and $P\left(|ts| \succ T|IF_w^{-1}\right)$. The term $P_{IF_w^1}$ indicates the probability of the first column of Table 1 i.e., the CF of N_1 under the probability of + 1 IF of N_w. This term can be expressed and bounded as follows,

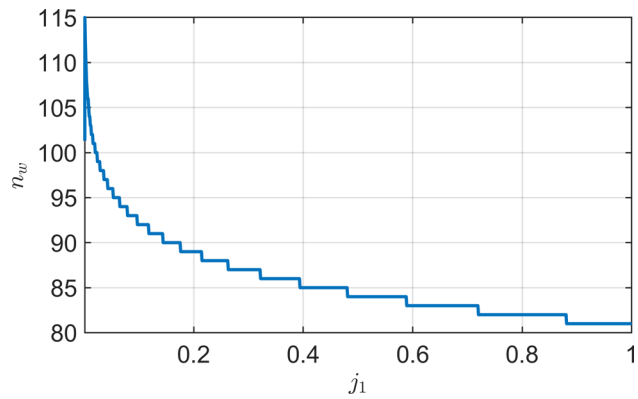

Fig. 10 Required n_w to achieve allocated $P_{IF_w^1}$

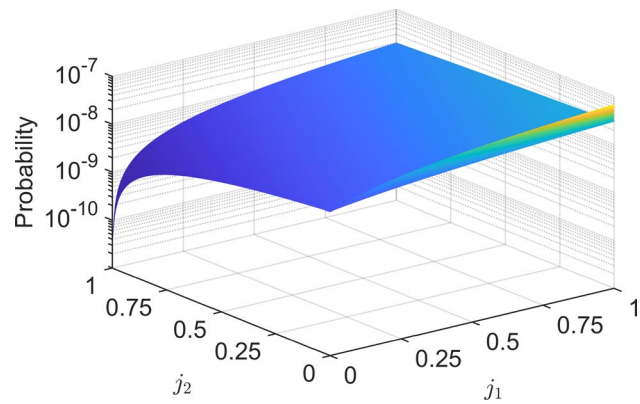

Fig. 11 P_{IF} allocation as a function of j_1 and j_2

$$P_{IF_w^1} = P(CF_1|IF_w^1)P\left(IF_w^1\right) \le P\left(IF_w^1\right) = P\left(\frac{1}{2} < \left|v_w - N_w\right| < \frac{3}{2}\right) \tag{22}$$

where $P\left(IF_w^1\right)$ represents the probability of + 1 IF of N_w. Different from the single threshold method, the overbounding of IF events is saved from considering the N_1 estimation as shown in (22), and $P_{IF_w^{-1}}$ can be bounded by the similar technique. Therefore, the bounding process for $P_{IF_w^1}$ and $P_{IF_w^{-1}}$ can be expressed by the following inequalities,

$$P_{IF_w^1} \le \Phi\left(\frac{\frac{3}{2}}{\hat{\sigma}_{cn}}\right) - \Phi\left(\frac{\frac{1}{2}}{\hat{\sigma}_{cn}}\right) \tag{23}$$

$$P_{IF_w^{-1}} \le \Phi\left(\frac{-\frac{1}{2}}{\hat{\sigma}_{cn}}\right) - \Phi\left(\frac{-\frac{3}{2}}{\hat{\sigma}_{cn}}\right) \tag{24}$$

Then, the allocated $P_{IF_w^1}$ and $P_{IF_w^{-1}}$ can be bounded by averaging among a sufficient number of epochs. The required n_w to achieve the allocated $P_{IF_w^1}$ as a function of j_1 is shown in Fig. 10.

Figure 10 indicates that increasing the probability allocated on $P_{IF_w^1}$ leads to a decrease in the required n_w needed to achieve the desired value of $P_{IF_w^1}$. Specifically, when j_1 increases from 0 to 1, the required n_w decreases from 115 to 81.

The last term in P_{FA} computation is $1 - P_{CF} - P_{IF_w^1} - P_{IF_w^{-1}}$. Given that $P_{IF_w^1}$ and $P_{IF_w^{-1}}$ are considered negligible in comparison to P_{CF}, this term can be bounded by $1 - P_{CF}$. Consequently, it is necessary to ensure that $1 - P_{CF}$, or equivalently, P_{IF}, is bounded by the allocated probability as shown in Fig. 11. As the values of j_1 and j_2 rang from 0 to 1, the allocated probability to P_{IF} varies from 10^{-10} to 10^{-7}.

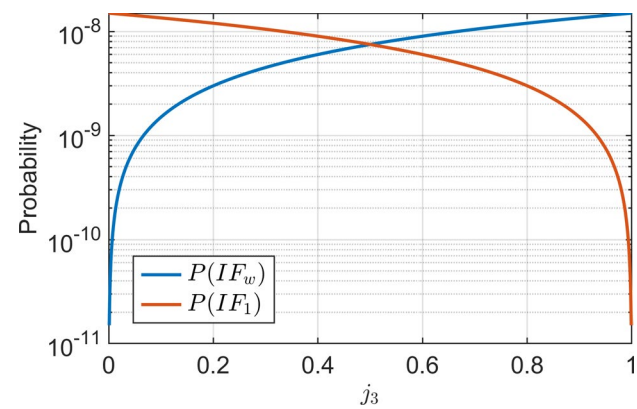

Fig. 12 Risk allocation as a function of j_3 given $j_1 = j_2 = 0.5$

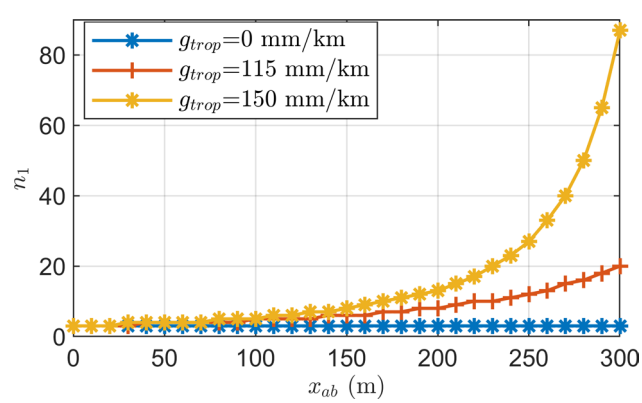

Fig. 13 n_1 with the multiple threshold method

With $P_{IF} = P\left(IF_w\right) + P\left(IF_1\right) - P\left(IF_w\right)P\left(IF_1\right)$, another factor of j_3 is defined to explore the optimal allocation between $P\left(IF_1\right)$ and $P\left(IF_w\right)$,

$$P(IF_w) = j_3 P_{IF} \tag{25}$$

where j_3 is limited as $0 \le j_3 \le 1$. The risk allocation between $P(IF_w)$ and $P(IF_1)$ is shown in Fig. 12.

Under the assumption that $j_1 = j_2 = j_3 = 0.5$, n_w is obtained as 86 from (13). With various g_{trop} and x_{ab}, n_1 is searched for from (14) to satisfy allocated $P(IF_1)$. The resultant x_{ab} is shown in Fig. 13.

Bounding risk of missed detection

The upper bound for P_{MD} with the multiple threshold method under the faulty hypothesis can be expressed as follows,

$$P_{MD} \le P(|ts| \prec T|CF)P_{CF} + P\left(|ts| \prec T|IF_w^1\right)P_{IF_w^1} + P\left(|ts| \prec T|IF_w^{-1}\right)P_{IF_w^{-1}} + \left(1 - P_{CF} - P_{IF_w^1} - P_{IF_w^{-1}}\right) \tag{26}$$

where the first three terms represent P_{MD} under CF, IF_w^1 and IF_w^{-1} events, and the last term bounds P_{MD} due to IF events beyond IF_w^1 and IF_w^{-1}.

The MD regions under CF, IF_w^1 and IF_w^{-1} events are illustrated in Fig. 14 by the grey areas,

The induced bias in test statistics under IF_w^1 and IF_w^{-1} in Table 1 interacts with the ionosphere anomaly under the faulty hypothesis. By either enhancing or weakening the influence of ionosphere anomaly in test statistics, the computation of $P\left(|ts| \prec T|IF_w^1\right)$ and $P\left(|ts| \prec T|IF_w^{-1}\right)$ is greatly complicated. With already constrained risks of $P_{IF_w^1}$, $P_{IF_w^{-1}}$ in P_{FA} bounding, the middle two terms in (26) are bounded by $P\left(|ts| \prec T|IF_w^1\right)P_{IF_w^1} \le P_{IF_w^1}$ and $P\left(|ts| \prec T|IF_w^{-1}\right)P_{IF_w^{-1}} \le P_{IF_w^{-1}}$, respectively. Based on these bounds, the P_{MD} can be further bounded by,

$$P_{MD} \le P(|ts| \prec T|CF)P_{CF} + \left(1 - P_{CF}\right) \tag{27}$$

where the second term $1 - P_{CF}$ is already bounded by the allocated probability from P_{FA}. Therefore, it suffices to bound only the first term, $P(|ts| \prec T|CF)P_{CF} \le P(|ts| \prec T|CF)$, to satisfy a required P_{MD}. Similar to the single threshold method, the minimum x_{ab} to bound $P(|ts| \prec T|CF)$ is computed by,

$$x_{ab} \ge \frac{\lambda_1^2 D_{ga}}{(\lambda_5^2 - \lambda_1^2)Er}\left[\Phi^{-1}\left(1 - \frac{P(|ts| \succ T|CF)}{2}\right) + \Phi^{-1}(1 - P(|ts| \prec T|CF))\right]\sigma_{ts} \tag{28}$$

The upper limit of D_{ga} and lower limit of Er are used for meeting the P_{MD} requirements.

With j_1 and j_2 determined, the allocation of risk on $P(|ts| \succ T|CF)$ and $P(|ts| \prec T|CF)$ can be obtained using (18) and (27). Subsequently, the minimum x_{ab} can be computed as a function of j_1 and j_2, as shown in Fig. 15.

Figure 15 indicates that the minimum x_{ab} is mainly determined by j_2, and it increases from 368 to 405 m as j_2 increases from 0 to 1. On the other hand, j_1 has little effect on the minimum x_{ab} as $P_{IF_w^1}$, determined by j_1, is negligible (less than 10^{-8}) compared to $P(|ts| \prec T|CF)$, which is on the order of 10^{-6}.

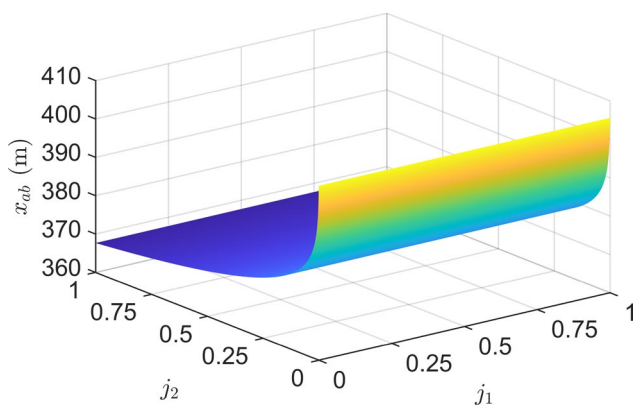

Fig. 15 x_{ab} versus j_1 and j_2 with the multiple threshold method

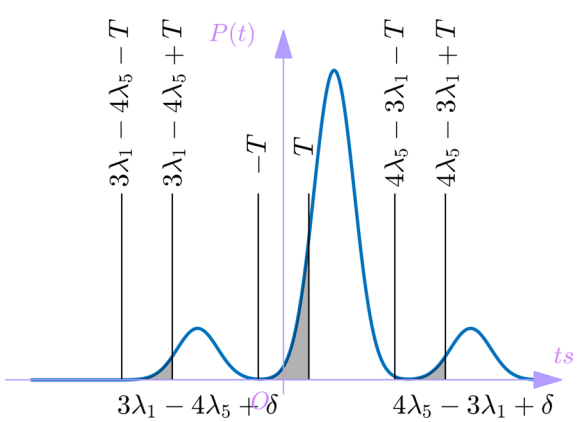

Fig. 14 Missed detection regions with the multiple threshold method, the grey areas represent the MD regions

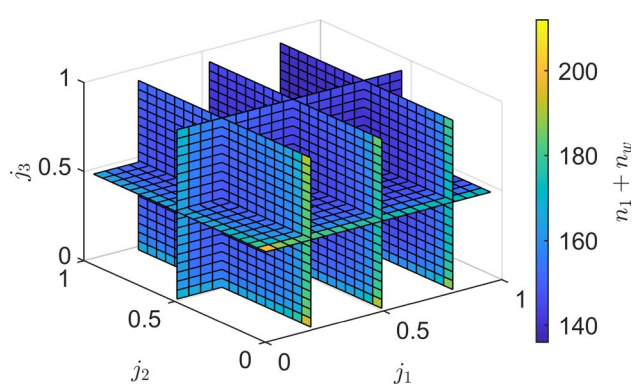

Fig. 16 Total epochs required for averaging with the multiple threshold method

In addition to the baseline length, the required number of epochs for averaging, i.e., $n_w + n_1$, also needs to be considered. The relationship between $n_w + n_1$ and allocation parameters j_1,j_2, and j_3 is shown in Fig. 16. The value of n_1 is obtained to bound the probability allocated to P_{IF} considering the maximum g_{trop} of 115 mm/km. Unlike the single threshold method, n_w is obtained to satisfy both $P(IF_w)$ and $P_{IF_w^1}$. Through Fig. 15, the minimum total epochs required for averaging is found to be 136 (t_a of 544 s assuming a time constant of 2 s), and the corresponding required threshold and baseline length to meet P_{FA} and P_{MD} requirements are 4.88 cm and 368.4 m, respectively. Similar to the single threshold method, the maximum baseline length of 473.6 m is determined by limiting $\left|\delta_{trop}\right| < \frac{1}{2}$. Note that the above conclusion is based on the maximum g_{trop} of 115 mm/km. Considering a potentially g_{trop} larger than 115 mm/km, the required averaging time will increase. In particular, when g_{trop} exceeds 149 mm/km, the required averaging time will be infinite. That is, N_1 cannot be correctly fixed since the troposphere-induced error in N_1 estimation is larger than 0.5, i.e., $\left|\delta_{trop}\right| > \frac{1}{2}$. The summary of probability allocation and the determination of overbounding parameters are illustrated in Fig. 17.

Due to the tolerance of IF_W^1 and IF_W^{-1} events, the performance of IGM with the multiple threshold method outperforms the single threshold method in terms of required epochs and baseline length. However, it is important to note that MD might occur when the ionospheric anomaly causes bias in the test statistic that is close to the regions corresponding to IF_W^1 and IF_W^{-1} events. Specifically, this occurs when the bias falls between $4\lambda_5 - 3\lambda_1 \pm T$ or $3\lambda_1 - 4\lambda_5 \pm T$.

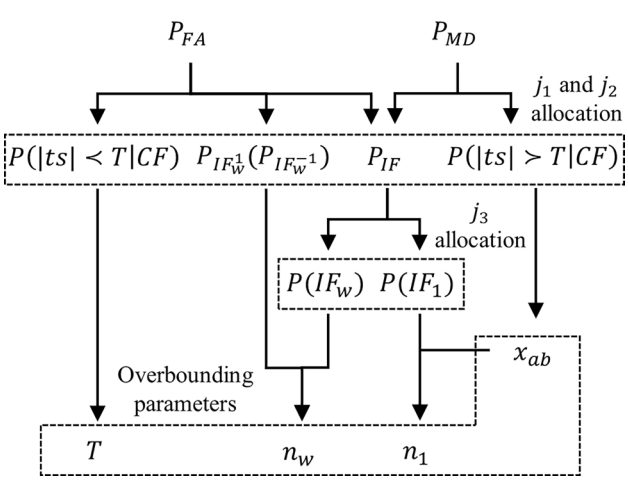

Fig. 17 Probability allocation and the bounding parameters with the multiple threshold method

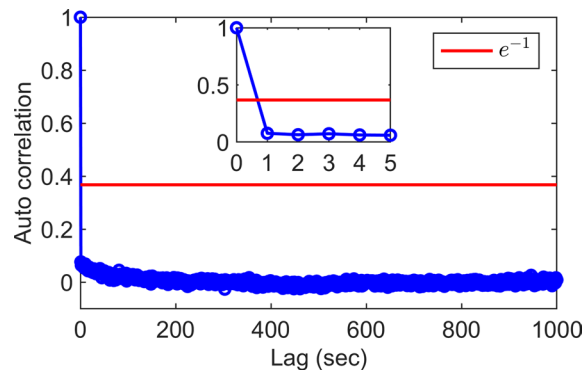

Fig. 18 Example of normalized autocorrelation for PRN 20 on April 21, 2022

Simulation results

The 1-Hz data were collected from Hong Kong Satellite Positioning Reference Station Network (SatRef). Since the time correlation of the double-differenced code measurements is crucial for ambiguity resolution, Fig. 18 shows the autocorrelation function for one of the processed satellites (PRN 20).

In order to find a time constant, a red horizontal line indicates exp(− 1) is drawn on the figure. The intersection between the red line and the autocorrelation function represents the first-order Gauss-Markov (GM) time constant assuming a first-order GM is an adequate model for multipath noise in double-differenced code measurements. The resultant time constant is 0.685 s. Therefore, a 2-s time constant is conservative for ambiguity resolution analysis.

Two stations HKQT and HKOH, with a baseline of 5 km, are used to form the test statistic of DDCP, WL DDCP, and GF DDCP. Due to the limitation of GPS L5 signals, measurements from L2 signals are used for the purpose of demonstration. Figure 19 shows the IGM with DDCP, WL DDCP,

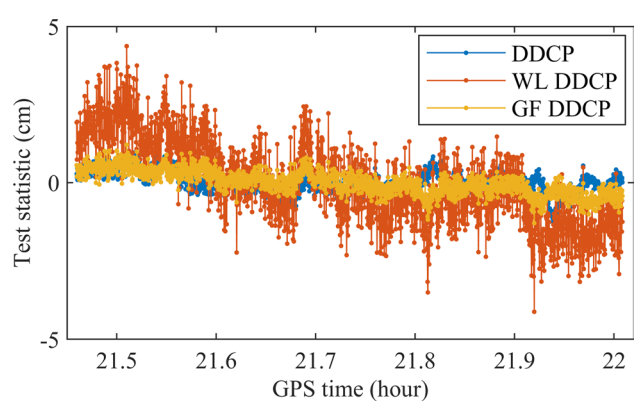

Fig. 19 IGM test statistics with SatRef data on April 21, 2022

and GF DDCP as the test statistics for PRN 32 (with PRN 26 as the reference satellite) from Universal Time 21:27 to 22:00. To reflect the general conditions, the day with normal atmospheric conditions are chosen, i.e., a dry day and the ionosphere is quiet.

As shown in Fig. 19, the noise level in WL DDCP is much larger than that of DDCP and GF DDCP. This is due to the enlarged residual troposphere error and noise in the WL DDCP. The Folded Cumulative Distribution Function (FCDF) method is widely applied to evaluate the residual error in the test statistics (Rife et al. 2006). In FCDF, the right tail likelihood represents the probability of exceeding a given x-axis value which is computed by 1 minus the CDF function. The FCDF for the empirical test statistics is computed and then compared to a bounding Gaussian CDF with a specific mean and standard deviation. The standard deviation of the bounding Gaussian needs to increase until the FCDF of the bounding Gaussian covers all empirical FCDF points. The bounding results for DDCP, WL DDCP, and GF DDCP are shown in Fig. 20.

As shown in Fig. 20, the bounding standard deviation of the WL DDCP is much larger than that of DDCP and GF DDCP. This is consistent with the results shown in Fig. 16. The resultant bounding standard deviation for DDCP, WL DDCP, and GF DDCP test statistics are 0.44, 1.45, and 0.42 cm, respectively. Since the residual geometry-related errors are eliminated by the GF DDCP, the magnitude of bounding standard deviation of GF DDCP is the smallest among DDCP, wide-lane DDCP, and GF DDCP. Therefore, it demonstrates that the proposed IGM is a promising substitute for the existing IGMs which apply DDCP or wide-lane DDCP as test statistics.

The chosen period in Fig. 19 is a dry day since no rainfall is recorded on this day and the relative humidity is not very high (78%) according to the Hong Kong Observatory. The residual tropospheric delay is believed to be small. The standard deviation of DDCP is slightly larger than that of GF DDCP might be due to the residual ephemeris errors. For comparison, the result of a wet day is shown in Fig. 21. The GNSS data of PRN 32 are collected on August 10, 2022. According to the Hong Kong Observatory, this day is recorded with heavy rainfall.

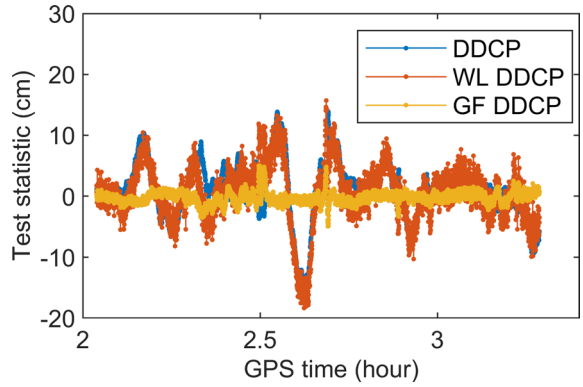

Fig. 21 IGM test statistics with SatRef data on August 10, 2022

As shown in Fig. 21, due to the residual tropospheric error caused by the heavy rainfall, the magnitudes of DDCP and WL DDCP are much larger than that of GF DDCP. Therefore, the proposed GF DDCP is more robust against humid conditions.

In addition, the ionospheric condition for the chosen period in Fig. 22 is quiet (the value of Dst is smaller than 50 nT and the Kp index is 3). In addition, this period is not affected by the scintillation induced by the equatorial plasma bubble (EPB) since the EPB only occurs after sunset. For comparison, we showed the test statistic results in Fig. 21 with PRN 7 on April 11, 2013. It is recorded that PRN 7 on this day is severely affected by the ionospheric scintillation (scintillation index is larger than 0.7) which is caused by the EPB during the midnight (Saito et al. 2017).

As shown in Fig. 22, under the effect of scintillation, the test statistics would increase significantly. Furthermore, the WL DDCP and GF DDCP would jump abnormally due to

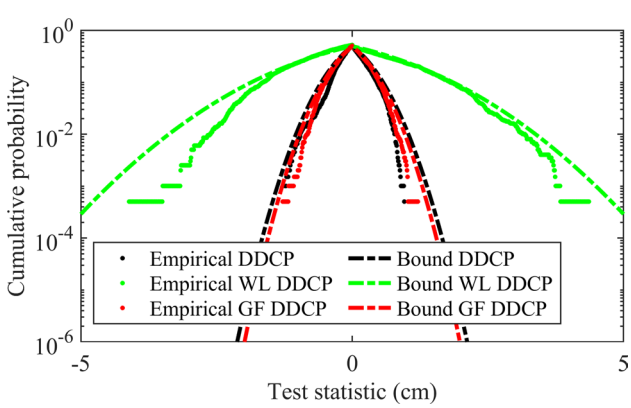

Fig. 20 Over-bounding Gaussian curves for IGM test statistic

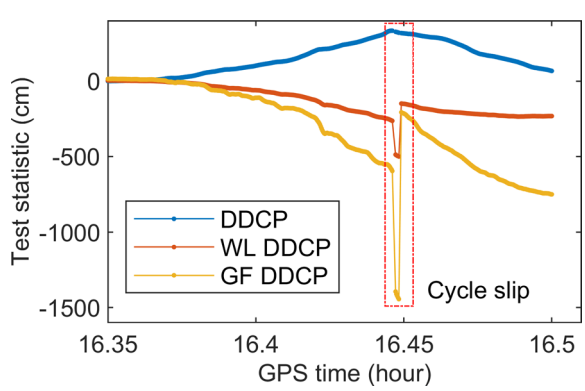

Fig. 22 IGM test statistics with SatRef data on April 11, 2013

the cycle clip of the L2 frequency carrier phase measurements. It should be noted that this numerical result is only used for the purpose of comparison. The bounding standard deviation of test statistics requires data from testbeds with the multipath limiting antenna.

Conclusion

The current IGMs use L1 DDCP or WL DDCP measurements to detect threatening ionospheric gradients caused by ionospheric anomalies. However, the residual tropospheric error may degrade the monitor performance by inducing extra risks under extreme weather conditions. To overcome this limitation, a GF IGM using the difference between L1 and L5 DDCP measurement is proposed to eliminate the tropospheric error from the test statistic. To resolve the ambiguity term in the test statistic, the integer ambiguity method is designed. In order to bound the risk of wrong ambiguity fix, a single threshold and a multiple threshold method are proposed with residual tropospheric error considered. The maximum residual tropospheric error is treated as a bias considering the maximum tropospheric gradient of 115 mm/km. The required averaging period and baseline length are derived to bound the risks in terms of P_{FA} and P_{MD}. With no introduced error from ambiguity resolution to test statistics, the required averaging period and baseline length are obtained as $t_a = 612$ s and $x_{ab} = 371.7$ m with the single threshold method, and $t_a = 544$ s and $x_{ab} = 384.4$ m with the multiple threshold method. Therefore, the integer ambiguity method is a preferred choice to achieve comparable performance with the existing method, which uses t_a of 337 s and x_{ab} of 600 m to meet P_{FA} of 10^{-8} and P_{MD} of 10^{-6} (Patel et al. 2020). In addition, the simulation results demonstrate that the GF IGM test statistics contains less noise than the current IGMs due to the elimination of residual tropospheric and ephemeris errors. Overall, the proposed IGM is a promising candidate to detect threatening ionospheric gradients for safety of life applications. The benefit is especially obvious for those areas with humid weather and extreme weather conditions.

Acknowledgements This research is funded by University Grants Committee / Research Grants Council (Grant Nos. 25202520; 15214523) and National Natural Science Foundation of China (Grant No. 42004029). These supports are gratefully acknowledged.

Authors' contributions YJ conceived of the presented idea. WL developed the theory and analytical methods. YJ supervised the findings of this work. All authors discussed the results and contributed to the final manuscript.

Funding Open access funding provided by The Hong Kong Polytechnic University. This research is funded by University Grants Committee/Research Grants Council (Grant Nos. 25202520; 15214523) and National Natural Science Foundation of China (Grant No. 42004029).

Availability of data and materials The GNSS dataset analyzed during the current study are available in the Hong Kong Geodetic Survey Services website (https://www.geodetic.gov.hk/en/index.htm).

Declarations

Conflict of interests The authors declare no conflict of interest.

Consent to participate Not applicable.

Ethics approval Not applicable.

Open Access This article is licensed under a Creative Commons Attribution 4.0 International License, which permits use, sharing, adaptation, distribution and reproduction in any medium or format, as long as you give appropriate credit to the original author(s) and the source, provide a link to the Creative Commons licence, and indicate if changes were made. The images or other third party material in this article are included in the article's Creative Commons licence, unless indicated otherwise in a credit line to the material. If material is not included in the article's Creative Commons licence and your intended use is not permitted by statutory regulation or exceeds the permitted use, you will need to obtain permission directly from the copyright holder. To view a copy of this licence, visit http://creativecommons.org/licenses/by/4.0/.

References

Alexander K, Mcdonald J, Johnson B (2014) Observed nominal atmospheric behavior using Honeywell's GAST D ionosphere gradient monitor. In: Proceedings on ION Navigation System Panel, CAT II/III Subgroup, Montreal, Canada

Belabbas B, Meurer M (2012) Carrier phase and code based absolute slant ionosphere gradient monitor for GBAS. In: Proceedings on ION GNSS 2012, Nashville, TN, pp 2201–2208

Brenner M, Liu F (2010) Ranging source fault detection performance for category III GBAS. In: Proceedings of ION GNSS 2010, Institute of Navigation, Portland, OR, pp 2618–2632

Circiu MS, Meurer M, Felux M, Gerbeth D, Thölert S, Vergara M, Enneking C, Sgammini M, Pullen S, Abtreich F (2017) Evaluation of GPS L5 and Galileo E1 and E5a performance for future multifrequency and multiconstellation GBAS. J Inst Navig 64(1):149–163. https://doi.org/10.1002/navi.181

Felux M, Circiu MS, Lee J, Holzapfel F (2017) Ionospheric gradient threat mitigation in future dual frequency GBAS. Int J Aerosp Eng 2017:1–10. https://doi.org/10.1155/2017/4326018

Felux M, Circiu MS, Belabbas B, Meurer M, Stanisak M, Milner C, Jiang Y, Guilbert A, Lipp A (2015) Concept for a dual frequency dual constellation GBAS. In: Proceeding on ION GNSS 2015, Institute of Navigation, Tampa, Florida, pp 1519–1525

Guilbert A, Milner C, Macabiau C (2017) Characterization of tropospheric gradients for the ground-based augmentation system through the use of numerical weather models. J Inst Navig 64(4):475–493. https://doi.org/10.1002/navi.205

Harris M, Murphy T, Saito S (2011) Further validation of GAST D ionospheric anomaly mitigations. In: Proceedings on ITM 2011, Institute of Navigation, San Diego, CA, USA, pp 942–949

Huang J, van Graas F, Cohenour C (2008) Characterization of tropospheric spatial decorrelation errors over a 5-km baseline. J Inst Navig 55(1):39–53. https://doi.org/10.1002/j.2161-4296.2008.tb00417.x

Huang J, van Graas F (2006) Comparison of tropospheric decorrelation errors in the presence of severe weather conditions in different areas and over different baseline lengths. In: Proceedings

on ION GNSS 2006, Institute of Navigation, Fort Worth, Texas, USA, pp 2769–2787

Hwang PY, McGraw GA, Bader JR (1999) Enhanced differential GPS carrier-smoothed code processing using dual-frequency measurements. J Inst Navig 46:127–137. https://doi.org/10.1002/j.2161-4296.1999.tb02401.x

Jiang Y (2020) Ephemeris monitor with ambiguity resolution for CAT II/III GBAS. GPS Solut 24:116–122. https://doi.org/10.1007/s10291-020-01028-4

Jiang Y, Milner C, Macabiau C (2017) Code-Carrier divergence for dual frequency GBAS. GPS Solut 21(2):769–781. https://doi.org/10.1007/s10291-016-0567-4

Jiang Y, Li W, Zhang H (2023) An efficient fault detection and exclusion method for ephemeris monitoring. Remote Sens 15(13):3259. https://doi.org/10.3390/rs15133259

Jing J, Khanafseh S, Chan FC, Langel S, Pervan B (2012) Detecting ionospheric gradients for GBAS using a null space monitor. In: Proceedings on IEEE/ION PLANS 2012, Institute of Navigation. Myrtle Beach, SC, USA, pp 1125–1133

Jing J, Khanafseh S, Langel S, Pervan B (2014) Detection and isolation of ionospheric fronts for GBAS. In: Proceedings on ION GNSS+ 2014, Institute of Navigation, Tampa, Florida, USA, pp 3526–3531

Khanafseh S, Langel S (2011) Implementation and experimental validation of cycle ambiguity resolution with position domain integrity risk constraints. J Inst Navig 58(1):45–58. https://doi.org/10.1002/j.2161-4296.2011.tb01791.x

Khanafseh S, Yang FC, Pervan B, Pullen S, Warburton J (2012) Carrier phase ionospheric gradient ground monitor for GBAS with experimental validation. J Inst Navig 59(1):51–60. https://doi.org/10.1002/navi.3

Khanafseh S, Pervan B (2008) A new approach for calculating position domain integrity risk for cycle resolution in carrier phase navigation systems. In: Proceedings on IEEE/ION PLANS, Institute of Navigation, Catamaran, CA, USA, pp 583–591. https://doi.org/10.1109/PLANS.2008.4570101

Khanafseh S, Patel J, Pervan B (2017) Ephemeris monitor for GBAS using multiple baseline antennas with experimental validation. In: Proceedings on ION GNSS 2017, Institute of Navigation, Portland, Oregon, USA, pp 4197–4209

Lee J, Morton YTJ, Lee J, Moon H, Seo J (2017) Monitoring and mitigation of ionospheric anomalies for GNSS-based safety critical systems: a review of up-to-date signal processing techniques. IEEE Signal Process Mag 34(5):96–110. https://doi.org/10.1109/MSP.2017.2716406

Luo M, Pullen S, Dennis J, Konno H, Xie G, Walter T, Enge P, Dattabarua S, Dehel T (2004) Ionosphere spatial gradient threat for LAAS: mitigation and tolerable threat space. In: Proceedings on ION ITM 2004, Institute of Navigation, San Diego, CA, pp 490–501

Marini-Pereira L, Pullen S, Moraes ADO, Sousasantos J (2021) Ground-based augmentation systems operation in low latitudes—part 1: challenges, mitigations, and future prospects. J Aerosp Technol Manag. https://doi.org/10.1590/jatm.v13.1236

Patel J, Khanafseh S, Pervan B (2020) Detecting hazardous spatial gradients at satellite acquisition in GBAS. IEEE Trans Aerosp Electron Syst 56(4):3214–3230. https://doi.org/10.1109/TAES.2020.2969541

Pervan B, Chan FC (2003) Detecting global positioning satellite orbit errors using short-baseline carrier-phase measurements. J Guid Control Dyn 26(1):122–131

Pullen S, Park YS, Enge P (2009) Impact and mitigation of ionospheric anomalies on ground-based augmentation of GNSS. Radio Sci 44(1):1–10

Pullen S (2000) Summary of ionosphere impact on PT 1 LAAS: performance and mitigation options, Stanford University, Department of Aeronautics and Astronautics

Reuter R, Weed D, Brenner M (2012) Ionosphere gradient detection for Cat III GBAS. In: Proceedings on ION GNSS 2012, Institute of Navigation, Nashville, Tennessee, USA, pp 2175–2183

Rife J, Pullen S, Enge P, Pervan B (2006) Paired overbounding for non-ideal LAAS and WAAS error distributions. IEEE Trans Aerosp Electron Syst 42(4):1386–1395. https://doi.org/10.1109/taes.2006.314579

Saito S, Sunda S, Lee J, Pullen S, Supriadi S, Yoshihara T, Terkildsen M, Lecat F (2017) Ionospheric delay gradient model for GBAS in the Asia-Pacific region. GPS Solut 21(4):1937–1947. https://doi.org/10.1007/s10291-017-0662-1

van Graas F, Zhu Z (2011) Tropospheric delay threats for the ground based augmentation system. In: Proceedings on ITM 2011, Institute of Navigation, San Diego, CA, USA, pp 959–964

Yoon M, Lee J, Pullen S (2020) Integrity risk evaluation of impact of ionospheric anomalies on GAST D GBAS. J Inst Navig 67(2):223–234. https://doi.org/10.1002/navi.33

Publisher's Note Springer Nature remains neutral with regard to jurisdictional claims in published maps and institutional affiliations.

Wang Li is a Ph.D. candidate at The Hong Kong Polytechnic University. He received his M.S. in the School of Automation Science and Electrical Engineering from Beihang University in 2020. His research interests include GBAS, ionospheric characteristics, and ionospheric anomaly monitoring for GBAS.

Yiping Jiang obtained her Ph.D. from the University of New South Wales in 2014 and is an Assistant Professor at The Hong Kong Polytechnic University. Her research interests include precise positioning and integrity monitoring technologies. She currently lectures on Avionics Systems and Satellite Navigation for undergraduate and postgraduate students.